Geophysical Journal International

Geophys. J. Int. (2015) **203,** 1149–1163
GJI Seismology

doi: 10.1093/gji/ggv357

Extracting seismic attenuation coefficients from cross-correlations of ambient noise at linear triplets of stations

Xin Liu, Yehuda Ben-Zion and Dimitri Zigone*

Department of Earth Sciences, University of Southern California, Los Angeles, CA 90089-0740*, USA. E-mail: liu409@usc.edu*

Accepted 2015 August 21. Received 2015 August 17; in original form 2015 April 8

SUMMARY

We develop and apply an algorithm for deriving interstation seismic attenuation from cross-correlations of ambient noise recorded by linear arrays. Theoretical results on amplitude decay due to attenuation are used to form a linear least-square inversion for interstation Q_R values of Rayleigh surface waves propagating along linear arrays having three or more stations. The noise wave field is assumed stationary within each day and the interstation distances should be greater than the employed wavelength. The inversion uses differences of logarithmic amplitude decay curves measured at different stations from cross-correlation functions within a given frequency band. The background attenuation between noise sources and receivers is effectively cancelled with this method. The site amplification factors are assumed constant (or following similar patterns) in the frequency band of interest. The inversion scheme is validated with synthetic tests using ambient noise generated by ray-theory-based calculations with heterogeneous attenuation and homogenous velocity structure. The interstation attenuation and phase velocity dispersion curves are inverted from cross-correlations of the synthetic data. The method is then applied to triplets of stations from the regional southern California seismic network crossing the Mojave section of the San Andreas fault, and a dense linear array crossing the southern San Jacinto Fault zone. Bootstrap technique is used to derive empirical mean and confidence interval for the obtained inverse Q values. The results for the regional stations yield Q_R values around 25 for a frequency band 0.2–0.36 Hz. The results for the San Jacinto fault zone array give Q_R values of about 6–30 for frequencies in the range 15–25 Hz.

Key words: Time-series analysis; Interferometry; Seismic attenuation; Seismic tomography; Wave scattering and diffraction; Wave propagation.

1 INTRODUCTION

The ambient seismic noise contains rich information on structural properties between the recording stations (e.g. Weaver & Lobkis 2004; Campillo 2006). Empirical Green's functions for surface waves can be retrieved by cross-correlating continuous noise data at different sites (Shapiro & Campillo 2004). The phase and amplitude information in the empirical Green's function have various applications in seismology (e.g. Campillo *et al.* 2011; Lin & Ritzwoller 2011; Boué *et al.* 2014). For successful retrieval of empirical Green's function, the noise wave field should be diffuse and the noise sources should be isotropic and uncorrelated. In practical cases the noise field is not fully diffuse and often has strong directionality, leading to asymmetric cross-correlations and ambiguity in the derivation and interpretation of results (e.g. Weaver 2011). Despite these difficulties, there have been many successful applications of retrieving information on seismic velocities from cross-correlation of ambient noise (e.g. Shapiro *et al.* 2005; Zhan *et al.* 2014; Zigone *et al.* 2015). Group velocities can be derived with multiple filter analysis (MFA) techniques (e.g. Dziewonski *et al.* 1969; Herrmann 1973; Pedersen *et al.* 2003) while phase velocities can be measured from the phases of narrow-band filtered noise cross-correlation functions (e.g. Yao *et al.* 2006; Lin *et al.* 2008; Boschi *et al.* 2013).

Getting amplitude information and inferring attenuation coefficients (Q values) from noise cross-correlation data is considerably more difficult. Prieto *et al.* (2009) derived interstation attenuation by fitting ensemble averaged coherency (Aki 1957) as a function of interstation distance with a damped Bessel function. However, the method ignores the attenuation between the sources and stations and involves additional assumptions that limit its utility (e.g. Tsai 2011; Weaver 2013; Liu & Ben-Zion 2013). Weaver (2013) proposed a method for deriving attenuation from linear array of at least five stations based on the radiative transfer equation and stationary phase approximation (Snieder 2004). Applying the radiative transfer equation to both sides (causal and anticausal) of synthetic linear arrays, Weaver (2013) estimated the attenuation coefficients together with site amplification factors and confidence intervals from

* Now at: Department of Meteorology and Geophysics, University of Vienna, Vienna, Austria.

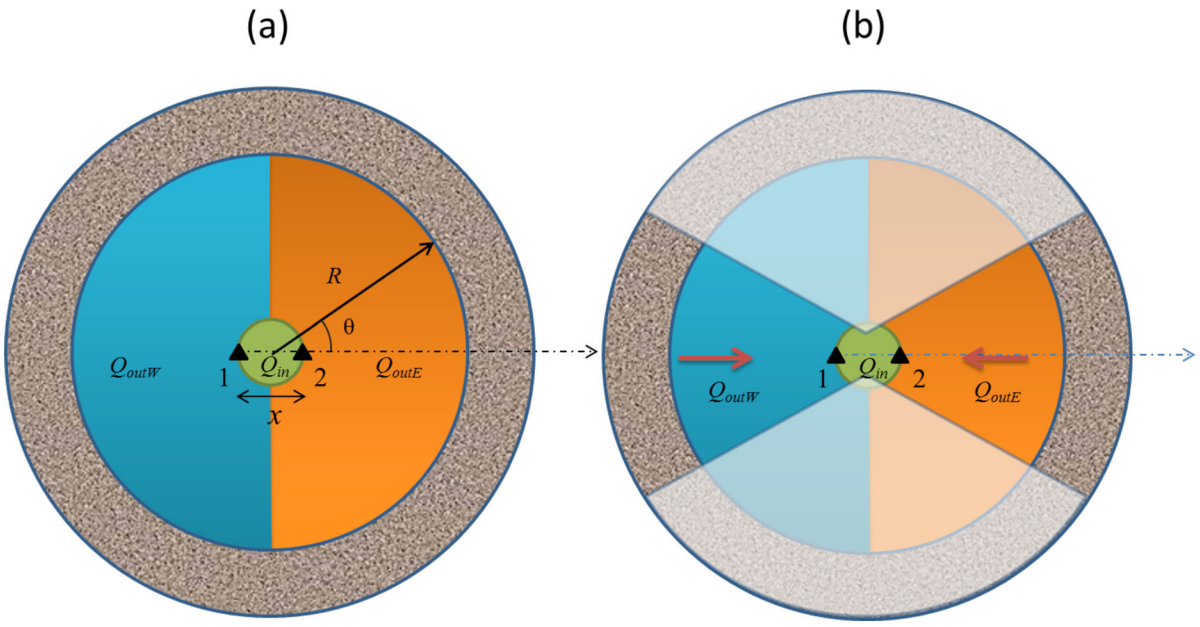

Figure 1. (a) Illustration of the 2-D geometry for random point noise sources in a ring (grey), attenuation structure (blue, orange and green areas described below), and station location (black triangles). The two stations are symmetric about the centre of the geometry. The interstation region (green) and the west and east outer regions are characterized by quality factor $Q_{\rm in}$, $Q_{{\rm out}W}$ and $Q_{{\rm out}E}$, respectively. (b) Under the stationary phase assumption, only the noise wavefields propagating near the interstation direction (end-fire lobes) have constructive interference on the cross-correlation.

synthetic data. Lin *et al.* (2012) derived site amplification factors by applying the eikonal equation with damping factors to earthquake data recorded by a 2-D array. To extend that study to noise cross-correlation data may require examination of amplitudes across the entire 2-D array, accounting for anisotropy of the noise sources and attenuation between the numerous sources and receivers (Galetti & Curtis 2012).

In this study, we develop an inversion algorithm based on previous theoretical results of Liu & Ben-Zion (2013) on effects of attenuation on noise cross-correlation between pairs of stations in a model with separate interstation Q value from that of the background attenuation. We apply the inversion formula to linear arrays of three stations (triplet), accounting for interstation attenuation values, background attenuation and site amplification factors. We perform numerical simulations with noise cross-correlation data described in terms of matrix multiplication and data covariance matrix. Synthetic noise cross-correlation data are generated from thousands of random noise sources, each of which is a sampling of the noise source probability space. Applying the inversion procedure to synthetic data shows that the three Q values between three stations can be reliably estimated for non-isotropic sources when the maximum noise intensity is oriented along the interstation direction. In contrast, only the Q value between the end stations can be reliably recovered for isotropic source distributions while the other two Q values are subjected to trade-offs. Applying the procedure to observed data, we analyse two linear arrays having different length scales. The first has three stations of the southern California regional network separated by about 35 km, while the second consists of six stations across the San Jacinto fault zone with interstation separation of about 25 m. For the former array we use a frequency band between 0.2 and 0.5 Hz and obtain $Q_{\rm R}$ values associated with Rayleigh waves around 25. For the latter array we use several frequency bands between 15 and 25 Hz and obtain $Q_{\rm R}$ values of about 6–30 with the lower values characterizing the fault damage zone. Bootstrapping the results with data of single days yields for most station pairs small confidence intervals of Q^{-1} values indicative of reliable estimations.

2 THEORY

We consider a pair of stations in a solid with three different attenuation coefficients characterizing the medium between the stations and the bounding regions to the left (west) and right (east) of the stations (Fig. 1a). Noise sources are assumed in the far field (denoted by the ring). Under stationary phase approximation (Snieder 2004), the cross-correlation amplitude is affected mostly by noise propagation along the interstation direction and noise sources in other directions have little contribution (Fig. 1b). This has been generally referred to as end-fire lobes in studies of noise correlations without attenuation (e.g. Roux *et al.* 2004; Gouédard *et al.* 2008). Below we combine this well-known phenomenon with the expression of noise cross-spectrum in dissipative medium (Liu & Ben-Zion 2013) to develop an inversion algorithm.

Based on Liu & Ben-Zion (2013) and derivations in Appendix, under the assumption that interstation distance x is greater than the wavelength λ ($2\pi x \gg \lambda$), the expected cross-spectrum between two stations can be approximated as

$$\begin{aligned}
\mathrm{E}\left\{\mathrm{C}_{u_1u_2}\left(-\frac{x}{2},\frac{x}{2};\omega\right)\right\} &= \pi\beta_1\beta_2\mathrm{B}(\omega)\sqrt{\frac{\mathrm{i}2c\,(\omega)}{\pi\omega x\varepsilon_W}} \\
&\times\exp\left[-\omega\left(\frac{R-x/2}{c\,(\omega)\,Q_{\rm out}W}+\frac{x}{2c\,(\omega)\,Q_{\rm in}}\right)\right]\exp\left[-\mathrm{i}\frac{\omega x}{c\,(\omega)}\right] \\
&+\pi\beta_1\beta_2\mathrm{B}(\omega)\sqrt{\frac{-\mathrm{i}2c\,(\omega)}{\pi\omega x\varepsilon_E}}\exp\left[-\omega\left(\frac{R-x/2}{c\,(\omega)\,Q_{\rm out}E}+\frac{x}{2c\,(\omega)\,Q_{\rm in}}\right)\right] \\
&\times\exp\left[\mathrm{i}\frac{\omega x}{c\,(\omega)}\right] \qquad (1)
\end{aligned}$$

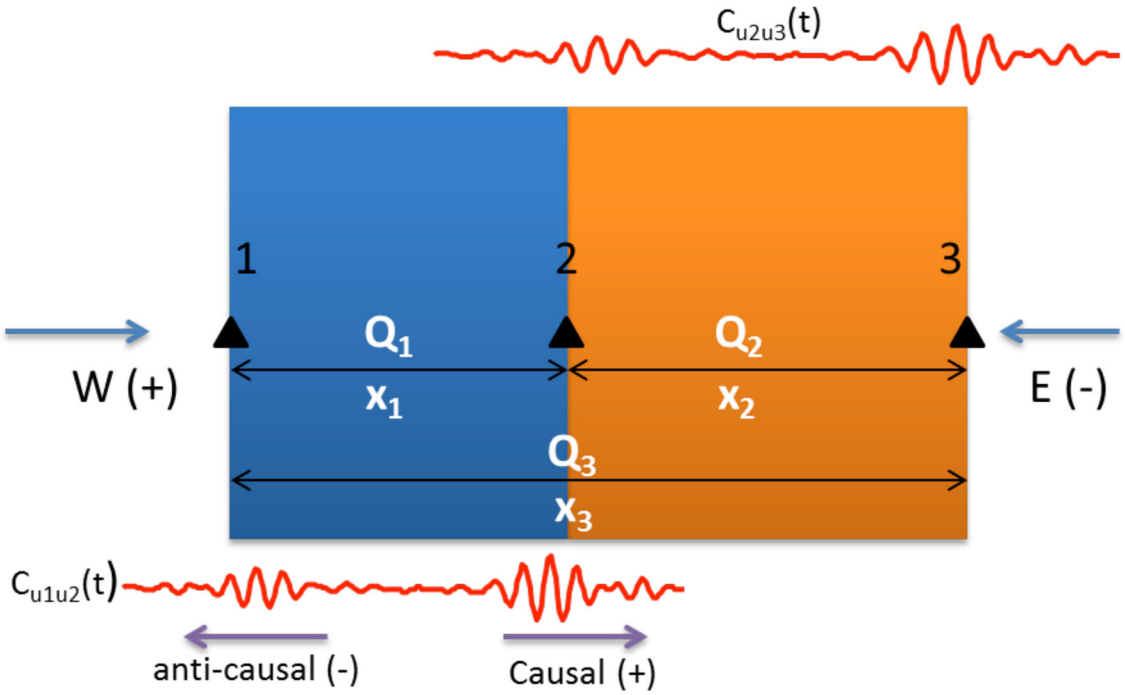

Figure 2. Schematic diagram for inverting attenuation from a linear array of three stations. Black triangles show the location of stations 1, 2 and 3 with interstation distances x_1, x_2 and x_3 and interstation quality factors Q_1, Q_2 and Q_3, respectively. Here Q_3 correspond to the apparent attenuation between stations 1 and 3. The distance between station 1 and 3, x_3, is the sum of x_1 and x_2. The background attenuation can be cancelled with this type of array as explained below eq. (2).

where R is the distance between far-field sources and origin, ω is angular frequency and $c(\omega)$ is phase velocity. Here β_1 and β_2 are real-value frequency-dependent site amplification factors at stations 1 and 2, respectively. The site amplification factors are assumed real; otherwise the phase velocity dispersion derived from cross-correlation will not be accurate. The two complex numbers $\epsilon_{\rm w}$ and $\epsilon_{\rm E}$ accounting for rotation of phase angle due to attenuation are defined below eq. (A2) of the Appendix.

The causal part (first two lines) of eq. (1) contains noise source spectral density $B(\omega)$, amplitude correction factor $\sqrt{\mathrm{i}2c\,(\omega)/\pi\omega x\varepsilon_W}$, an exponential decay term (attenuation term) and a phase term (the imaginary complex exponential). An intuitive interpretation of the attenuation term in eq. (1) is that the attenuation of the causal part of the cross-correlation function is only relevant to noise wave field propagating from the west along (nearly) the interstation direction, and vice versa. As a result, the exponential decay of the causal part is determined by the $Q_{\mathrm{out}W}$ and Q_{in} values between the western noise sources and two receivers along the end-fire lobe direction (Fig. 1b). The phase velocity can be extracted from the phase term multiplied by $\sqrt{i}$ (giving $\pi/4$ phase shift) with non-uniqueness because the phase angle is wrapped on an interval between $(-\pi, \pi)$.

A straightforward linear inversion can be formed by taking the ratios of amplitude cross-spectra functions in a given frequency band of different station pairs of a linear array. The simplest situation involves three stations on a line (Fig. 2), because the background attenuation term and noise source power spectral density $B(\omega)$ can be cancelled in this situation. The noise waveforms at three stations are denoted u_1, u_2 and u_3, respectively. The amplitudes may be measured on either the causal or anti-causal parts of the amplitude cross-spectra, and then corrected by dividing with the amplitude correction term $\sqrt{2c\,(\omega)/\pi\omega x\varepsilon_W}$ (We assume $\epsilon_{\rm w} \approx 1$ in realistic cases). Let $\widehat{\mathrm{C}}^{+}_{u_1u_2}(\omega)$, $\widehat{\mathrm{C}}^{+}_{u_2u_3}(\omega)$, $\widehat{\mathrm{C}}^{+}_{u_1u_3}(\omega)$ be the corrected amplitude decay curves of the causal cross-correlation functions of three station pairs. We form three linear least-square equations for the three attenuation factors

$$\begin{aligned}
\ln\widehat{\mathrm{C}}^{+}_{u_2u_3}(\omega) - \ln\widehat{\mathrm{C}}^{+}_{u_1u_3}(\omega) &= \frac{-\omega x_1}{2c_1\,(\omega)\,Q_1} + \gamma_{2/1}\\
\ln\widehat{\mathrm{C}}^{+}_{u_1u_3}(\omega) - \ln\widehat{\mathrm{C}}^{+}_{u_1u_2}(\omega) &= \frac{-\omega x_2}{2c_2\,(\omega)\,Q_2} + \gamma_{3/2}\\
\ln\widehat{\mathrm{C}}^{+}_{u_2u_3}(\omega) - \ln\widehat{\mathrm{C}}^{+}_{u_1u_2}(\omega) &= \frac{-\omega x_3}{2c_3\,(\omega)\,Q_3} + \gamma_{3/1},
\end{aligned} \tag{2}$$

where the relevant distances x and quality factors Q are defined in Fig. 2. Here $\gamma_{2/1}$, $\gamma_{3/2}$, $\gamma_{3/1}$ account for the natural logarithms of the ratios of corresponding site amplification factors (β values in eq. 1) and they are assumed to be constant in the frequency band used for inversion. Eq. (2) still holds if the site amplification factors at three stations are correlated with each other and can be removed by taking the ratio of them in eq. (2).

A Q value and a ratio of corresponding site amplification factors can be inverted from each expression of eq. (2) with simple linear least-square inversion in a chosen frequency band. The frequency band should be wide enough to allow for sufficient amplitude decay that exceeds random amplitude fluctuation. The inverted Q value only reflects the average amplitude decay within that frequency band. A similar version to eq. (2) defined for a noise wave field propagating from the west (assumed to be the causal part of the cross-correlation function), can be derived for noise wave field propagating from the east (anti-causal part of cross-correlation). We note that if the attenuation is strong enough, it may shift the phase velocity retrieved from the cross-correlation function. This can be observed from the complex coefficients ε_W and ε_E (eq. 1) which contain

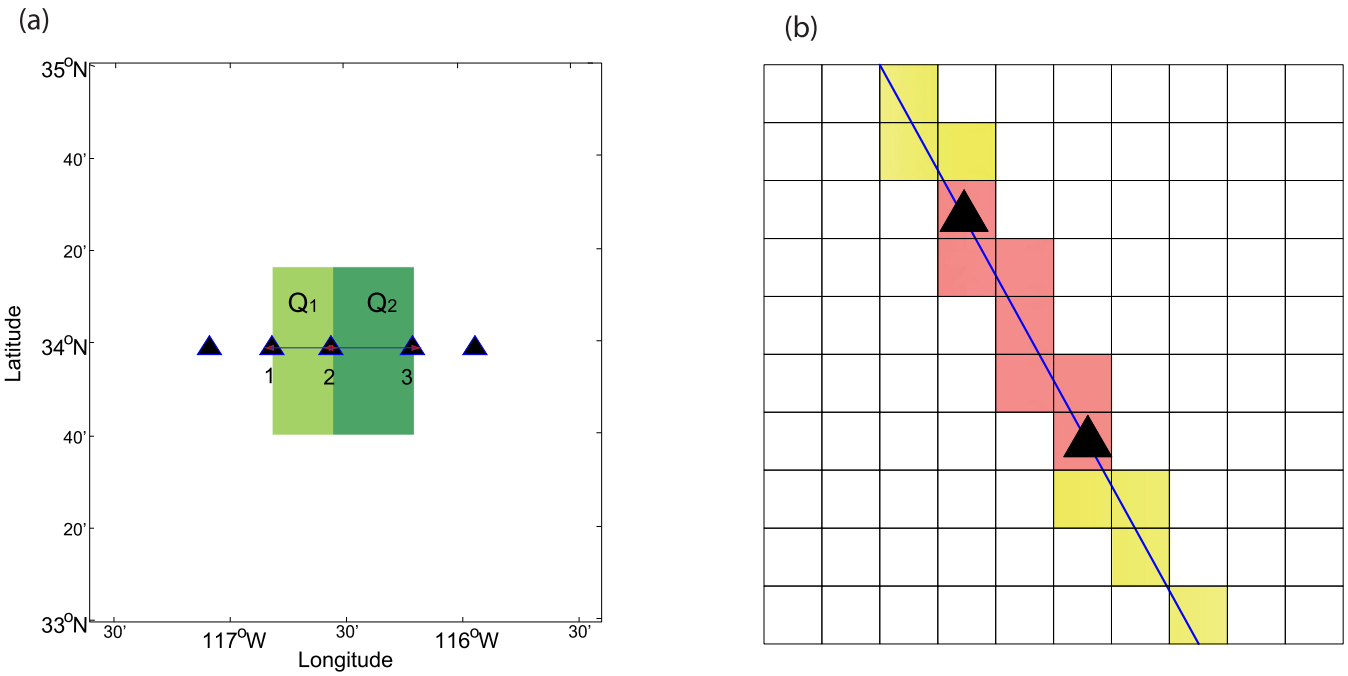

Figure 3. (a) Forward simulation geometry with heterogeneous attenuation. The black triangles show the station locations. The region between stations 1 and 2 has $Q_1 = 80$ and $x_1 = 24.2$ km; the region between stations 2 and 3 has $Q_2 = 30$ and $x_2 = 32.3$ km. Their weighted average attenuation between stations 1 and 3 is $Q_3 = 41$ with distance $x_3 = 56.5$ km. The background Q (white area) is 500. (b) Along-path attenuation and grid cells between two stations (black triangle). Each grid cell is defined with an attenuation Q value. Exponential decay of amplitude is computed by taking into account each grid cell along the ray path.

attenuation quality factors and rotate the phase angle in the causal and anti-causal parts. However, the attenuation has to be very strong (e.g. $Q \sim 2$–3) to cause a noticeable phase shift in the cross-correlation function. Therefore it is safe to assume $\epsilon_{\rm w} = \epsilon_{\rm E} = 1$ in most practical cases.

3 NUMERICAL SIMULATIONS OF NOISE WAVEFORMS AND INVERSION OF Q VALUES

The discrete version of noise spectrum produced by far-field noise sources at k receivers (eq. 1 in Liu & Ben-Zion 2013) is

$$\begin{bmatrix} u_1(\omega) \\ \vdots \\ u_k(\omega) \end{bmatrix} = \frac{1}{\sqrt{R}} \times \begin{bmatrix} \exp\left[-\frac{i\omega x_1(\theta_1)}{\tilde{c}(\omega)}\right] & \cdots & \exp\left[-\frac{i\omega x_1(\theta_n)}{\tilde{c}(\omega)}\right] \\ \vdots & \ddots & \vdots \\ \exp\left[-\frac{i\omega x_k(\theta_1)}{\tilde{c}(\omega)}\right] & \cdots & \exp\left[-\frac{i\omega x_k(\theta_n)}{\tilde{c}(\omega)}\right] \end{bmatrix} \begin{bmatrix} s_1(\omega) \\ \vdots \\ s_n(\omega) \end{bmatrix}, \quad (3a)$$

or

$$U = PS, \quad (3b)$$

where P is the propagation matrix, U is a vector that contains the spectrum at each station and S is a random vector of noise sources at different azimuth angle θ. In (3a), θ_1 to θ_n are equally spaced azimuth angles (used to approximate an integral) of n assumed sources with respect to the centre of the array. The source–receiver distance from source m to receiver l is $x_m(\theta_l)$. The inverse complex phase velocity is defined as $1/\tilde{c}(\omega) = (1 - i\,\mathrm{sgn}(\omega)/2Q(\omega))/c(\omega)$ where Q is the (potentially space-dependent) attenuation quality factor. The geometric spreading factor is approximated by $1/\sqrt{R}$ where R is the average source–receiver distance (Fig. 1).

Assuming a stationary ambient noise process, the covariance matrix of the random spectrum data from all receivers is,

$$\mathrm{Cov}U = P\mathrm{Cov}(S)\,P^{+}, \quad (4)$$

where Cov(S) is the covariance matrix of the noise sources and the dagger operator denotes conjugate transpose. For equipartitioned noise wavefield, any two different noise sources are uncorrelated, which implies that Cov(S) is a diagonal matrix. For isotropic source distribution, Cov(S) is the identity matrix. For the data covariance matrix at frequency ω, each non-diagonal entry represents the cross-spectrum of two stations at that frequency while each diagonal entry represents auto-spectrum. Synthetic data can be generated from eqs (3a,b) and (4) by either (i) repeatedly compute data covariance matrix UU^{+} from random noise source vector S and then average the results, or (ii) compute Cov$U$ directly from a known source covariance matrix Cov(S). The former can simulate finite length of data while the latter is directly computing the ensemble average of cross-spectrum. The propagation matrix P can be pre-computed to save time.

The forward wave propagation calculations are based on ray theory. We first discretize the region of interest. In the following we use grid spacing of 4.04 km and overall grid size of 202 km × 222 km (Fig. 3a). We focus on $Q_{\rm R}$ values associated with attenuation of Rayleigh waves, although for brevity we sometime just use Q to denote $Q_{\rm R}$. The region between stations 1 and 2 is defined with attenuation $Q_1 = 80$ and distance $x_1 = 24.2$ km while the rectangle between stations 2 and 3 is given $Q_2 = 30$ and $x_2 = 32.3$ km. The averaged Q_3 value between stations 1 and 3 is 41 with distance $x_3 = 56.5$ km. The background attenuation is assumed to

be $Q_{out} = 500$. We apply a UTM projection to convert spherical coordinates to local Cartesian coordinates for the region. For a ray path between a source–receiver pair, only the portion within the stations is discretized to account for heterogeneous attenuation by adding up the contribution of each grid cell (Fig. 3b). The portion of ray path outside the local grid is assumed to travel in homogeneous dissipative media with time delay and amplitude loss computed along the great circle path.

We simulate 20 000 noise sources assumed to be uncorrelated stochastic sources located 11° (distance in spherical degrees) away from the centre of the grid. We consider both non-isotropic sources with maximum intensity direction in the west along the interstation direction (Fig. 4a, max/min = 1.5) and isotropic source distributions. The estimated cross-spectra and autospectra (power spectra) are computed by 8000 iterations. The frequency band is 0–0.86 Hz with sample interval of 0.005 Hz. The computation takes about 11 hours on a single CPU.

As a prior information for the attenuation inversion, phase velocity curves for the three stations in Fig. 3(a) are first inverted from real part of the cross-spectra. Fig. 4(b) shows the inverted phase velocity for all three station-pairs for the case with non-isotropic source distribution. The isotropic case yields very similar phase velocity results. The inverted phase velocity curves are very similar to the model phase velocity except that the map projection produces small errors in distance calculations. The causal part of the cross-correlation (red waveform in Fig. 4c) is isolated by applying a Turkey window defined by velocity bounds between 1 and 6 km s^{-1} on the cross-correlation (blue waveform in Fig. 4c). Amplitude decay curves are measured from the amplitude cross-spectra of the causal correlation function, which represent noise wave propagating from west to east. Then the decay curves are corrected according to eq. (1) by removing the amplitude correction term (Fig. 4d, in logarithmic scale).

Attenuation Q values are inverted according to eq. (2). For non-isotropic noise source distribution, Fig. 4(e) shows results for the LHS of eq. (2) as three relative decay curves giving the differences between the logarithms of the measured-corrected amplitudes of the three cross-correlation functions. Each expression in eq. (2) is solved with linear least-square inversion for a Q value in the frequency range from 0.2 to 0.5 Hz. The inverted Q values for this case agree well with the forward model parameters in Fig. 3(a). For isotropic source distribution, the averaged attenuation Q_3 between stations 1 and 3 is recovered with good precision (Fig. 4f). However, there are some trade-offs between the inverted Q_1 and Q_2 values. One explanation is that the cross-correlation function between stations 1 and 3, $\widehat{C}_{u_1u_3}(t)$, should be symmetric as predicted by the stationary phase approximation under symmetric background attenuation. However, the actual simulated data have slight asymmetry since the noise waveforms propagating outside the end-fire lobes do not cancel out completely because of the asymmetric interstation attenuation (Q_1, Q_2) between stations 1 and 3. An inaccurate $\widehat{C}_{u_1u_3}(t)$ produces errors in Q_1 and Q_2 derived using eq. (2).

The synthetic tests show that the best scenario for this inversion method is non-isotropic noise source distribution (at least for the parameters used in this section), with maximum intensity aligned with the interstation direction and smoothly varying noise intensity. For isotropic source distribution, only the inverted average attenuation between stations 1 and 3 has good precision. In addition, because the aperture angle for the end-fire lobes decreases as interstation distance increases (Roux *et al.* 2004; Snieder 2004), the spacing between stations in the triplet should not be significantly different. Although the synthetic test is set up for a relatively low frequency range between 0.2 and 0.5 Hz (and corresponding relatively large station separation), the conclusions hold for higher frequencies and densely spaced arrays if $2\pi x \gg \lambda$ is satisfied.

4 INVERTING Q VALUES FOR A REGIONAL ARRAY

Using a similar technique, we derive Q_R values for the paths between a triplet of stations of the southern California seismic network. The three used stations, CHF-SBB2-LMR2, cross the Mojave section of the San Andreas fault (Fig. 5). The analysis is based on vertical component seismograms recorded from Julian day 50 to day 350 of year 2014. The chosen three stations are located in relatively simple crust outside large sedimentary basins (although station CHF is in a mountainous area). The interstation distances for CHF-SBB2, CHF-LMR2 and SBB2-LMR2 are 43.6, 73.3 and 29.7 km, respectively. Before pre-processing step, the instrument responses are removed, the raw waveforms are high-pass filtered with a lower cut-off frequency of 0.02 Hz and the sampling rate is decimated to 4 Hz. The pre-processing of the noise data includes glitch correction and removal of segments contaminated by earthquakes (see Zigone *et al.* 2015 for more details). However, in contrast to typical noise-based imaging studies no frequency whitening is applied to avoid amplitude distortion (e.g. Weemstra *et al.* 2014). The computed daily cross-correlations are stacked to obtain one combined cross-correlation for each station pair (Fig. 6a).

As a prior information for amplitude correction and attenuation inversion, phase velocity dispersion curves are computed from the symmetric component of the cross-spectra, which is the real part of eq. (1). As a post-correlation whitening step for phase velocity measurements, we normalize the stacked cross-spectra by the power spectra functions of both receivers (e.g. Aki 1957; Prieto *et al.* 2009) before phase velocity measurements. We adopt two methods for phase velocity analysis: (i) estimate and unwrap phase angle data measured on narrow-band filtered cross-correlation in time domain (e.g. Lin *et al.* 2008) and (ii) estimate phase angle data in frequency domain from the inverse Fourier transform of the causal part of cross-correlation (phase term in eq. 1). These two methods produce consistent results. The measured phase velocity curves are shown in Fig. 6(b); the dispersion curves intersect at two points since the phase velocity on the longest path (CHF-LMR2) is the weighted average of those on the two shorter paths (CHF-SBB2 and SBB2-LMR2) in the triplet.

In a second analysis step, the cross-spectral amplitude is measured by separating the causal and anticausal parts of unwhitened complex cross-spectra according to eq. (1). There are generally two ways of separating the two opposite propagating terms: (i) frequency domain Hilbert Transform of the bandpass filtered complex cross-spectra based on eq. (1) and (ii) time domain windowing on the causal part cross-correlation function followed by Fourier transform to frequency domain. The former has better resolution in the frequency domain but does not remove the correlation coda and requires that the cross-correlation function only contain the fundamental mode Rayleigh wave. The latter assumes that signals other than the fundamental Rayleigh wave travel at different speeds and therefore the fundamental Rayleigh wave mode can be isolated by windowing at predicted time interval (although different modes may overlap and can be hard to separate). However, the energy of the traveling wave in the causal part may suffer from leakage at the anti-causal part due to fast decaying ambient noise energy with

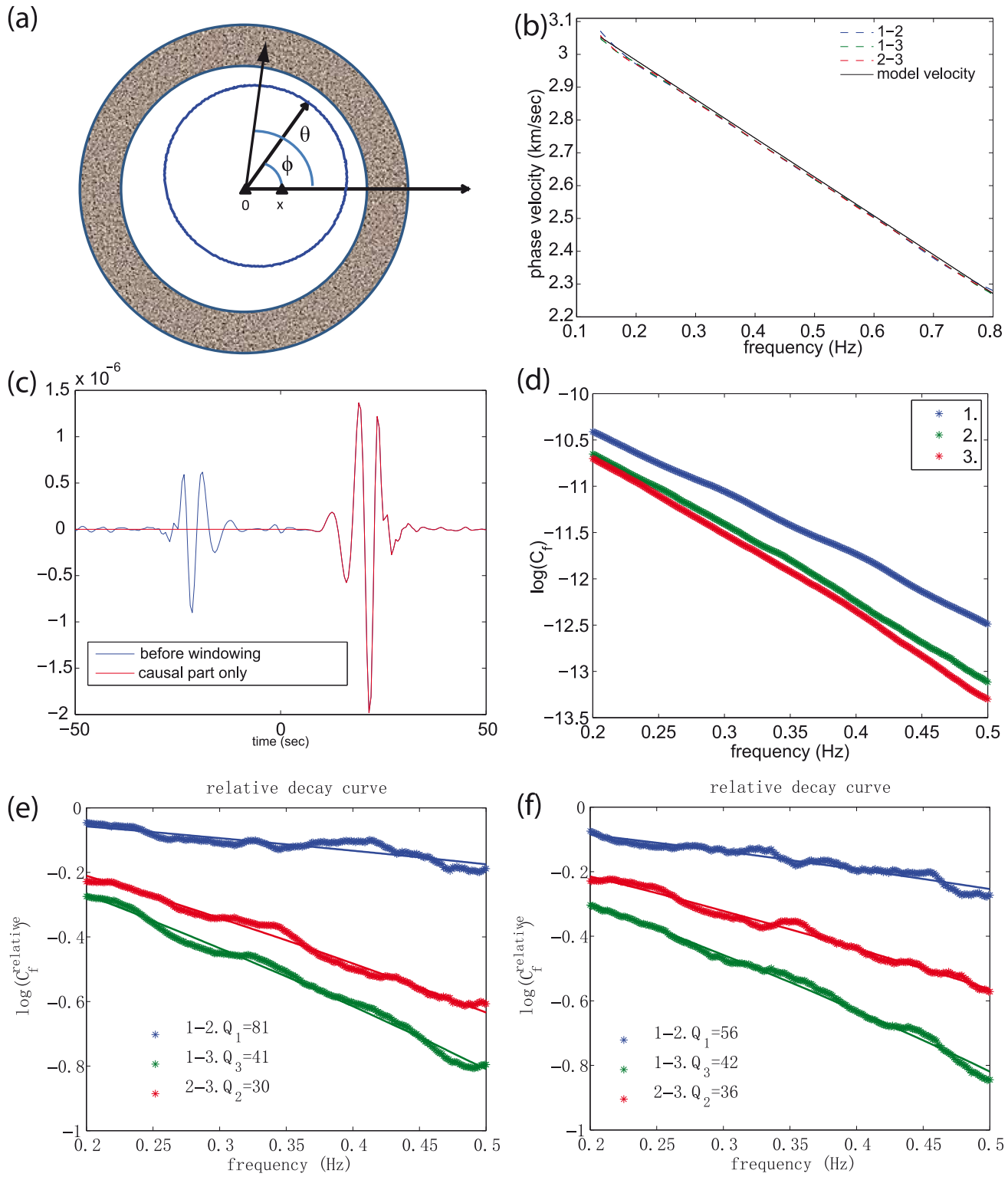

Figure 4. Geometry and results for the synthetic example. (a) Non-isotropic source distribution around two stations (black triangles): maximum intensity rotation angle ϕ and max/min ratio of noise intensity distribution. (b) Phase velocity inversion for three station pairs. Black line: model phase velocity; dashed line: inverted phase velocity. There is good agreement between model and inverted results. (c) Cross-correlation for stations 1 and 3 before windowing (blue) and the causal part of the cross-correlation after applying a Turkey window (red) based on lower and upper bounds of phase velocity (1–6 km s^{-1}). (d) Corrected amplitude measurement (log scale) as a function of frequency for the causal parts of the 3 cross-correlation functions in a non-isotropic source case with max/min = 1.5 and $\phi = 180$ (maximum intensity in the West). The colours indicate the station (see legend on the panel). (e) Relative decay curve as a function of frequency for the non-isotropic source distribution defined in panel (d). The curves are differences between the logarithmic amplitude curves in panel (d). The inverted Q values indicated in the panel are very close to the model values in Fig. 3(b). Best-fitting curves are plotted as solid lines with the same colour as data. (f) Same as (e) for an isotropic source distribution. The inverted Q_3 is very close to the assumed value, while the inverted Q_2 and Q_1 are less accurate because of trade-offs.

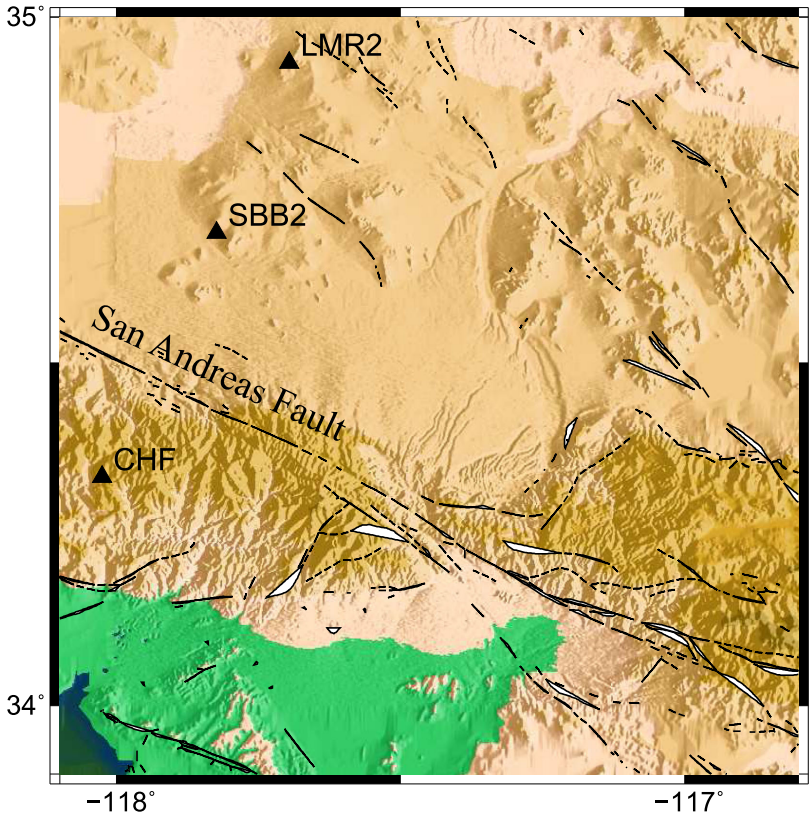

Figure 5. A map for a triplet of stations, CHF-SBB2-LMR2 (black triangles), of the regional southern California network. Black lines indicate fault traces. The green and yellow show low and high elevation, respectively.

frequency, small interstation distances and *P* wave incidence below the array. Therefore, we use the former method for triplets with much stronger surface wave packets than body waves and the latter method for cases with weaker surface wave packets that need to be separated from body waves.

For amplitude measurements with data of the regional triplet, we apply Wiener filter to reduce the noise level in the cross-correlations. We first define a signal window by phase velocity bounds between 1 and 6 km s^{-1}. The noise window starts 5 s after the signal window and has a total duration of 50 s. The Wiener filter is a minimum mean-square estimator of the surface wave packet signal. Because of the strong ocean microseism peak around 0.16 Hz, the amplitude of cross-spectra above 0.2 Hz decays very fast and the cross-correlation is dominated by 7 s waves. Therefore we deconvolve the autocorrelation of the two stations from the cross-correlation following the approach of Aki (1957) before Wiener filtering and convolve them back after the Wiener filtering.

The corrected amplitude decay curves for the three station pairs, based on the stacked cross-spectra for random resampling of 300 d, are shown in Fig. 6(c). We smooth the amplitude decay curves with a running average smoothing parameter of 0.05 Hz. The frequency band used for the linear least-square inversion is between 0.2 and 0.36 Hz. The relative amplitude decay curves and inverted Q values are shown in Fig. 6(d). To estimate the ensemble mean and confidence interval of the inverted Q values, we bootstrap the 300 d and get distributions of three inverse Q values (Fig. 6e). The inverted results suggest that CHF-SBB2 has slightly stronger attenuation ($Q_1 \approx 21$, $1/Q_1 = 0.049 \pm 0.011$) than SBB2-LMR2 ($Q_2 \approx 32$, $1/Q_2 = 0.031 \pm 0.013$), possibly due to damaged rocks around the San Andreas Fault, but the difference is not highly significant statistically. The average attenuation between CHF and LMR2 is $Q_3 \approx 25$ ($1/Q_3 = 0.040 \pm 0.006$) associated with a narrow confidence interval.

5 INVERTING Q VALUES FOR A FAULT ZONE ARRAY

Here we derive Q_R values for the paths between six stations of a dense linear array that crosses the southern San Jacinto Fault zone at site JF (Fig. 7). As in the pre-processing stage for the three stations of the regional network, we avoid pre-whitening, perform glitch corrections and remove segments affected by earthquakes. The cross-correlations are computed on the radial RR component instead of the vertical ZZ component in order to minimize body *P* wave phases (e.g. Hillers *et al.* 2013) which could affect the amplitude measurements. The phase velocity dispersion curves are derived from the stacked cross-correlations as discussed in the previous section. We compute signal-to-noise ratio (SNR) for daily cross-correlations from a set of 80 d for the year 2012 and select 34 d with highest SNRs for all six stations. The amplitude decay curves are measured as in the previous section, using either frequency domain Hilbert transform or time domain windowing, except that Wiener filter is not applied to triplets with very high SNR (e.g. JFS2-JFS1-JF00). We assume that each one of the 34 d is an independent observation of the amplitude cross-spectra and that the ambient noise field is relatively stationary within each day (so that the cross-correlation can converge). A bootstrapping technique is used to estimate empirical mean value and confidence interval of the attenuation Q^{-1} by randomly resampling the 34 d of cross-correlations.

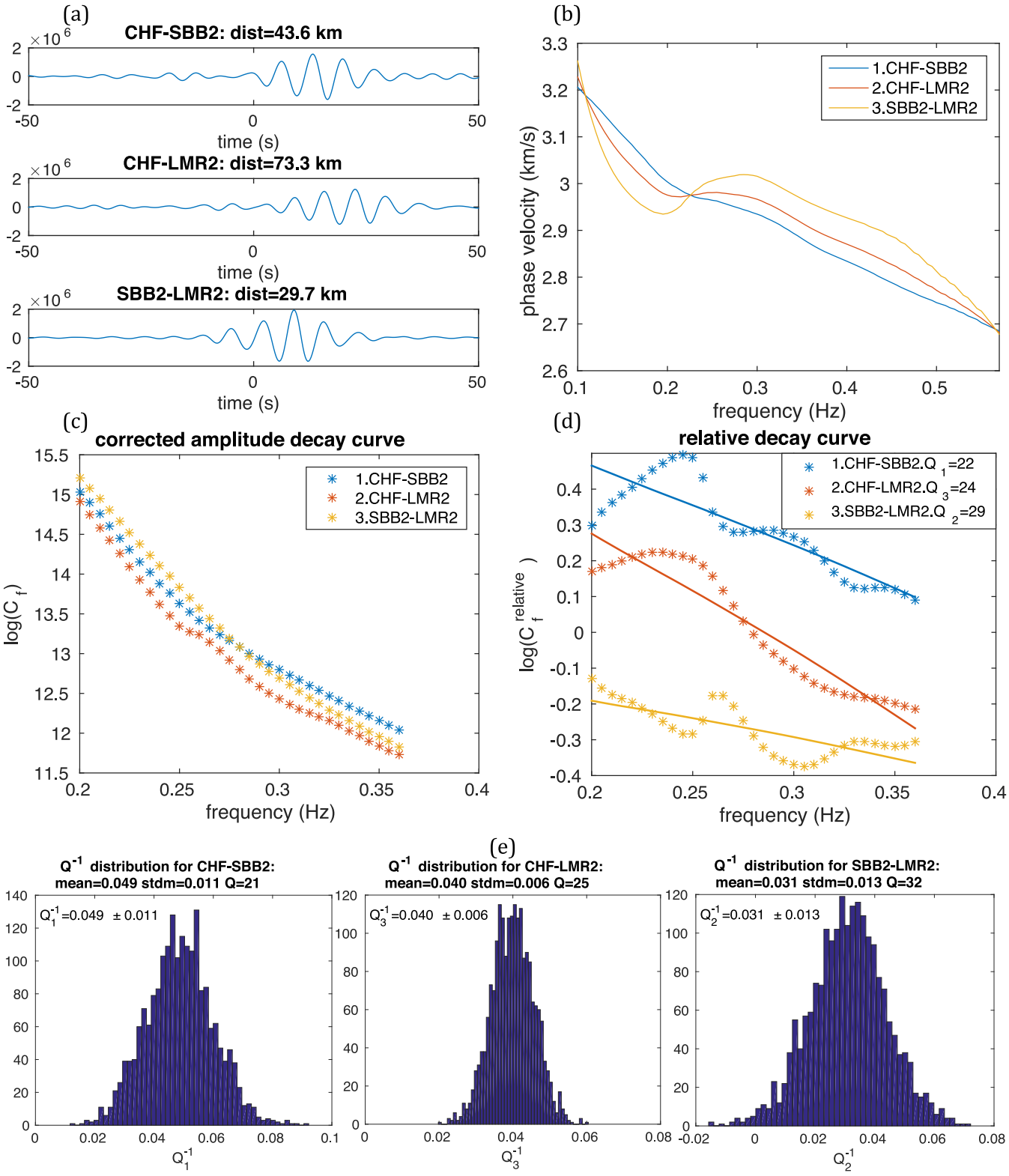

Figure 6. Cross-correlation functions, phase velocity curves, amplitude measurements and inverse Q distribution for CHF-SBB2-LMR2 (see station locations in Fig. 5). (a) Cross-correlations for CHF-SBB2-LMR2. Distances between each pair of stations are shown in the titles. (b) Phase velocity dispersion curves. (c) Corrected amplitude decay curves for the three correlation functions. The frequency range is 0.2–0.36 Hz and is determined in relation to the interstation distance. (d) Relative amplitude decay curve and inverted Q_R values from a random resampling of 300 d in year 2012. Best-fitting curves are plotted as solid lines with the same colour as data. (e) Distribution of inverse Q values for the three station pairs based on bootstrapping statistics ($1/Q_1 = 0.049 \pm 0.011$; $1/Q_3 = 0.040 \pm 0.006$; $1/Q_2 = 0.031 \pm 0.013$).

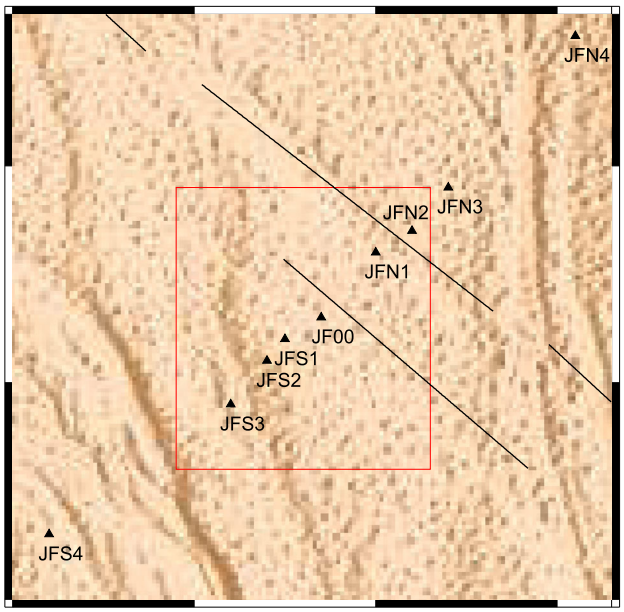

Figure 7. A map for the JF array with nine broad-band stations (black triangles) across the San Jacinto Fault Zone. The black lines mark surface fault traces. The inversion for Q values is done for data by the six stations in the red square forming four station triplets.

The cross-correlations are one-sided for triplet JFS2-JFS1-JF00 (Fig. 8a), showing a strong non-isotropic source distribution or asymmetric background attenuation. The inverted phase velocity on the longest path JFS2-JF00 is about the average of those for the two shorter paths JFS2-JFS1 and JFS1-JF00 (Fig. 8b). The interstation distances are small, so the amplitude measurements are done on relatively high frequencies (20–25 Hz) to approximate the attenuation between stations. The amplitude curves (Fig. 8c) are measured by the frequency domain Hilbert transform approach and are corrected based on eq. (1). These curves are smoothed using a moving average method with a length of 10 Hz. The amplitude curves before smoothing have notable fluctuations on the semi-logarithm scale. This is probably because there are correlated noise sources and/or strong variation due to random scattering and random excitation of noise, and/or remaining small earthquakes (e.g. Ben-Zion *et al.* 2015) that cannot be completely removed by the pre-processing. The Q values are inverted from the relative decay curves (Fig. 8d) using eq. (2) and a random resampling of 34 d of the cross-correlation results. Then the 34 d are randomly resampled 1000 times using bootstrap technique to create a set of Q^{-1} values from which the mean and standard deviation are calculated (Fig. 8e). The bootstrap results indicate that the segment between JFS2 and JF00 has strong attenuation ($Q_3 \approx 8$, $1/Q_3 = 0.120 \pm 0.005$), which probably results from the fault damage zone. The three cross-correlation functions show consistent asymmetry, suggesting that the Q values of two short segments JFS2-JFS1 ($Q_1 \approx 14$, $1/Q_1 = 0.071 \pm 0.026$) and JFS1-JF00 ($Q_2 \approx 6$, $1/Q_2 = 0.170 \pm 0.016$) are reliable as found in the synthetic test with non-isotropic source distribution.

The second triplet JFS2-JF00-JFN2 has larger interstation distance (Fig. 9a), the associated analysis uses a lower frequency range (15–20 Hz), and the phase velocity dispersion curves are more separated apart (Fig. 9b). The cross-correlation (Fig. 9a) is again asymmetric due to non-isotropic source distribution and attenuation/scattering. As a result, the inverted Q values should provide reliable estimates for the attenuation structure along the two shorter segments (JFS2-JF00 and JF00-JFN2). However, the SNR is not as good as for the first triplet JFS2-JFS1-JF00 due to the larger distance. The amplitude decay curve (Fig. 9c) is again measured in frequency domain Hilbert transform. The southern pair JFS2-JF00 has strong attenuation ($Q_1 \approx 11$, $1/Q_1 = 0.094 \pm 0.017$), while the northern pair JF00-JFN2 has higher phase velocity and its attenuation is not reliably determined ($1/Q_2 = -0.005 \pm 0.011$) with standard deviation twice as large as the absolute value of mean in the bootstrap distribution. The attenuation on the longest path JFS2-JFN2 is $Q_3 \approx 24$ ($1/Q_3 = 0.041 \pm 0.006$). The pair JFS2-JF00 also corresponds to the longest path (Q_3) in triplet JFS2-JFS1-JF00 (Fig. 8) and the inverted Q values for this segment in the two triplets are in good agreement. The minor difference comes from the shorter interstation distances and higher frequency band used in JFS2-JFS1-JF00 (Fig. 8) leading to $Q = 8$, compared to those used here for JFS2-JF00-JFN2 leading to $Q = 11$. These results suggest that the fault damage zone exists primarily to the SW of station JF00 (Figs 7–9). This is consistent with observations of fault zone trapped waves in that fault section (Qiu *et al.* 2015). We also note that the attenuation corresponding to the longest path is more accurate (smaller error of $1/Q_3$) than those of the two shorter segments.

For the two additional triplets, JFS3-JFS1-JFN1 and JFN2-JFN1-JFS1, the cross-correlations (panel a), relative decay curves (panel b) and bootstrap inverse Q distributions (panel c) are shown in Fig. 10 (frequency band use for the inversion is 15–25 Hz) and Fig. 11 (frequency band used for the inversion is 18–25 Hz), respectively. Because of the relatively large distance and strong body phase associated with JFS3-JFN1, we apply time domain windowing to localize the surface wave packet for amplitude measurements. The inverted Q values show that JFS3-JFS1 has stronger attenuation ($Q_1 \approx 5$, $1/Q_1 = 0.198 \pm 0.037$) than the northern segment JFS1-JFN1 ($Q_2 \approx 20$, $1/Q_2 = 0.049 \pm 0.018$), which is consistent with the previous two triplets. Interestingly, the Q values for JFN2-JFN1-JFS1 show also that the northern segment JFN2-JFN1 has weaker attenuation ($Q_1 \approx 31$, $1/Q_1 = 0.032 \pm 0.016$) compared to the southern segment JFN1-JFS1 ($Q_2 \approx 16$, $1/Q_2 = 0.064 \pm 0.009$). However, there are noticeable differences in the inverted Q values of JFN1-JFS1 from these two triplets, which is probably due to relatively low SNR and large interstation distances.

6 DISCUSSION

Deriving attenuation from ambient noise cross-correlation can provide important information on structural and wave propagation properties between recording stations. Based on theoretical results on amplitude decay of ensemble-averaged cross-correlations due to attenuation (Liu & Ben-Zion 2013), we develop an inversion algorithm to retrieve interstation Q_R values from cross-spectra of ambient noise data by using linear triplets of stations. For this particular geometry, the three cross-correlation functions share common noise sources and background attenuation in the causal (or anti-causal) direction. Using redundant information in the triplet and assuming that the coherent noise comes mainly from the end-fire lobe direction (with interstation distance > wavelength), the background attenuation, noise source spectra and site amplification can be removed from the analysis. This allows us to form a linear least-square inversion (eq. 2) for interstation Q values using cross-spectra in the same frequency band at the three station pairs. The site amplification factors of the three stations are assumed constant or following similar pattern in the used frequency range.

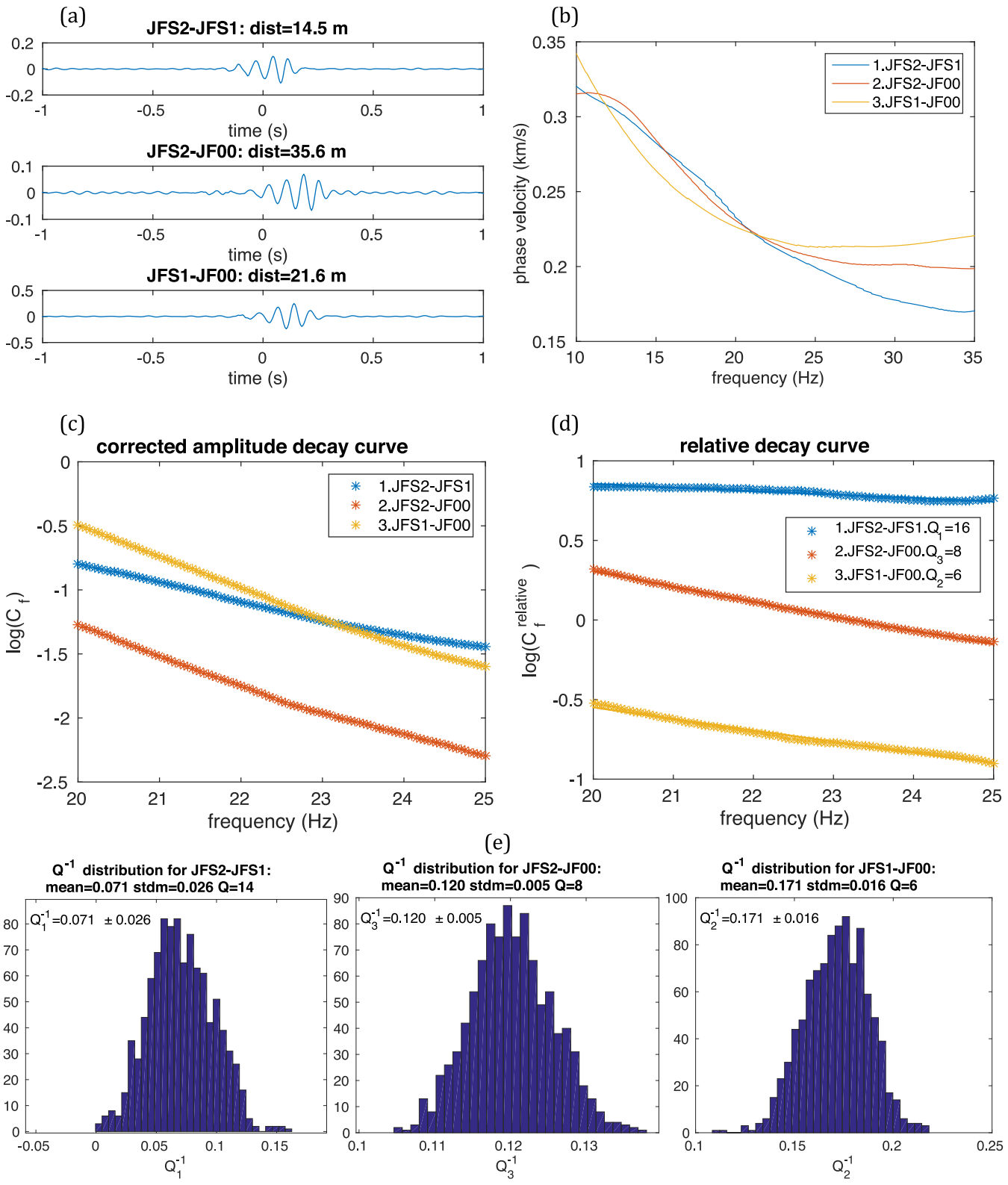

Figure 8. Cross-correlation functions, phase velocity curves, amplitude measurements and inverse Q distribution for JFS2-JFS1-JF00 (station locations are in Fig. 7). (a) Cross-correlations for JFS2-JFS1-JF00. Distances between each pair of stations are shown in the titles. (b) Phase velocity dispersion curves. (c) Corrected amplitude decay curves for three correlation functions. The frequency range is 20–25 Hz related to the small interstation distance. (d) Relative amplitude decay curve and inverted Q_R values from a random resampling of 34 d. Best-fitting curves are plotted as solid lines with the same colour as data. (e) Distribution of inverse Q values for three station pairs based on bootstrapping statistics ($1/Q_1 = 0.071 \pm 0.026$; $1/Q_3 = 0.120 \pm 0.005$; $1/Q_2 = 0.171 \pm 0.016$).

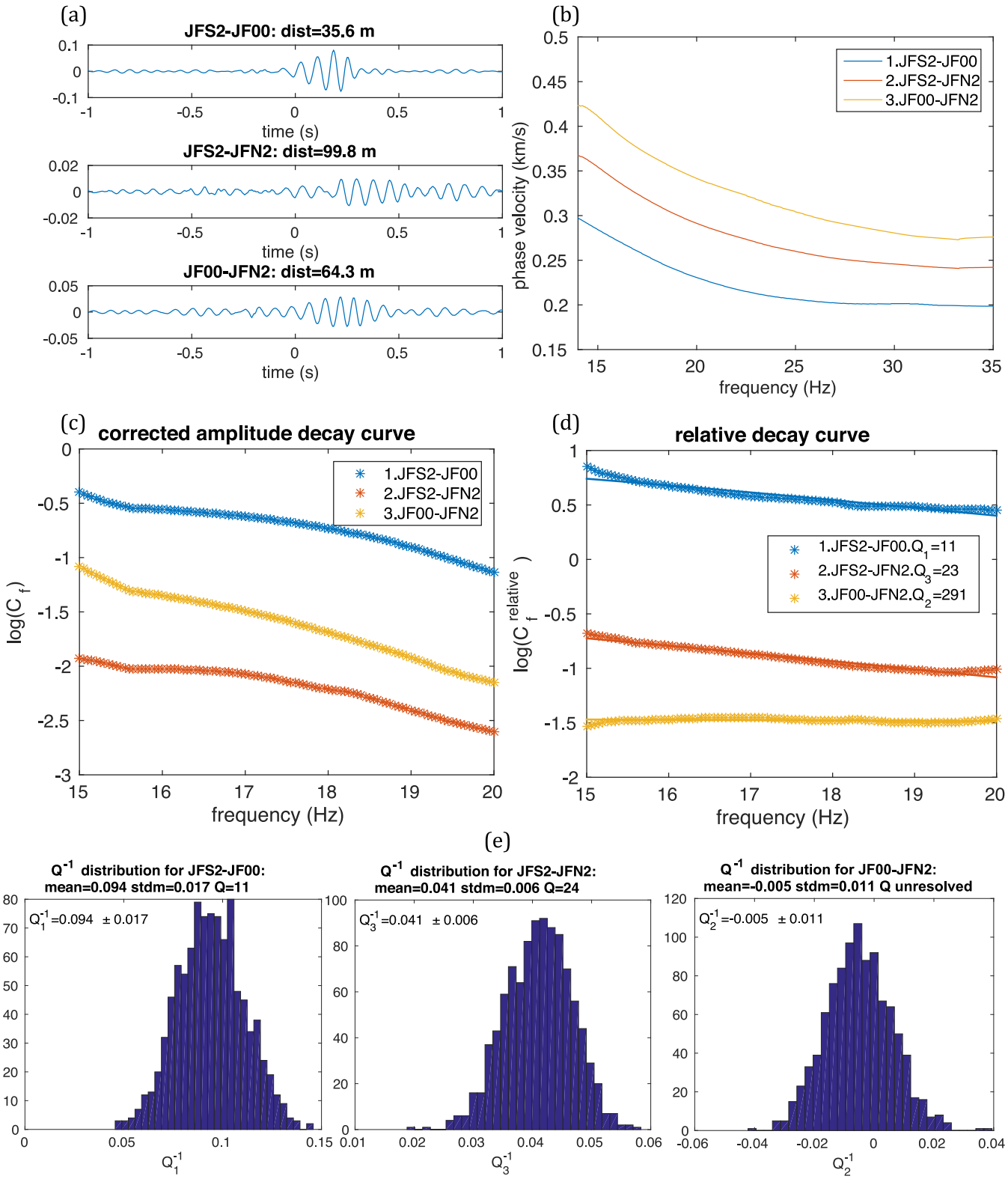

Figure 9. Cross-correlation functions, phase velocity curves, amplitude measurements and inverse Q distribution for JFS2-JF00-JFN2 (see Fig. 7 for station locations). (a) Cross-correlations for JFS2-JF00-JFN2. (b) Phase velocity dispersion curves. (c) Corrected amplitude decay curves on three correlation functions. The frequency range is 15–20 Hz related to the slightly larger interstation distance compare to the triplet JFS2-JFS1-JF00 in Fig. 8. (d) Relative amplitude decay curves and inverted attenuation Q values from random resampling of 34 d. Best-fitting curves are plotted as solid lines with the same colour as data. (e) Distribution of inverse Q_R values for three station pairs based on bootstrapping statistics ($1/Q_1 = 0.094 \pm 0.017$; $1/Q_3 = 0.041 \pm 0.006$; $1/Q_2 = -0.005 \pm 0.011$).

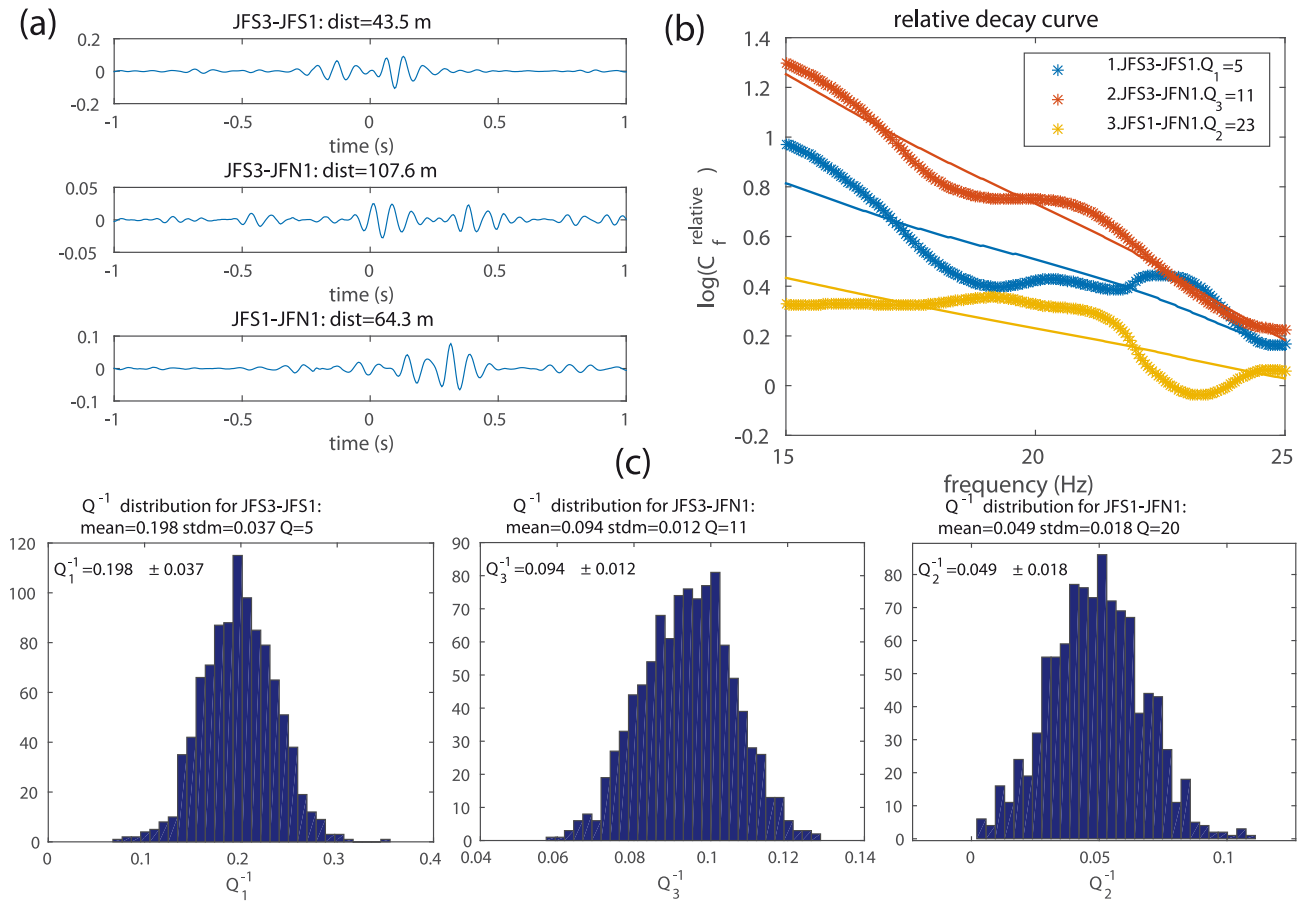

Figure 10. Cross-correlation functions, amplitude measurements and inverse Q distribution for triplet JFS3-JFS1-JFN1 (see locations in Fig. 7). (a) Cross-correlations for JFS3-JFS1-JFN1. (b) Relative amplitude decay curve. Best-fitting curves are plotted as solid lines with the same colour as data. The frequency range is 15–25 Hz. (c) Distribution of inverse Q values for the 3 station pairs in JFS3-JFS1-JFN1 based on bootstrapping statistics ($1/Q_1 = 0.198 \pm 0.037$; $1/Q_3 = 0.094 \pm 0.012$; $1/Q_2 = 0.049 \pm 0.018$).

The proposed method complements previous studies on deriving attenuation information between pairs of stations. In particular, Weaver (2013) developed a formulation for obtaining attenuation based on radiative transfer equation for linear array of at least four stations. The method is applied to narrow-band filtered cross-correlation functions in time domain and involves measuring the peak amplitude on both causal or anticausal part across the array to invert for attenuation coefficient and site amplification. The formulation of Weaver (2013) was proven theoretically and applied to real data, but it requires more stations and data (at least six good cross-correlation functions with both causal and anticausal parts) than the inversion proposed here. The basic equations in this paper and Weaver (2013) are consistent although they are obtained by different approaches; our results on amplitude and phase terms are derived in the frequency domain while Weaver (2013) provides the amplitude of narrow-band filtered noise cross-correlation in time. The causal part of eq. (1) agrees with eq. (1) of Weaver (2013) in that they both have exponential decay term, amplitude correction term (geometrical decay term in Weaver (2013)) and noise source intensity term.

Our inversion formula is validated with synthetic noise cross-correlations and is then applied to estimate Q values along linear arrays of two different scales in southern California. The synthetic test results suggest that the proposed method can better resolve Q values of the two inner station pairs for non-isotropic source distribution case with maximum intensity parallel with interstation direction than isotropic source distribution. This is likely because the noise waveforms propagating in the latter case outside the end-fire lobes do not cancel out each other sufficiently in heterogeneous dissipative medium. In application of the method to a station triplet within the regional southern California network with interstation distances of ∼35 km (Fig. 5), the frequency band for attenuation inversion is relatively low (0.20–0.36 Hz; slightly higher than the ocean microseism peak). The obtained Q_R values are ∼25 along the used triplet and likely reflect attenuation in the top 5 km of the crust. The depth is based on 1/3 of wavelength that the Rayleigh wave is most sensitive to (Nolet 1987). The Q_R values are significantly lower than the body wave Q_S ∼ 400 at 5 km depth estimated by Hauksson & Shearer (2006) based on *S*-wave spectra of earthquakes associated with a much higher frequency band.

Applying the inversion algorithm to six stations (four triplets) of a linear array with smaller interstation spacing (∼25 m) that crosses the San Jacinto fault zone (Fig. 7), we use higher frequencies in the range 10–25 Hz. The analysis involves four triplets (from JFS3 to JFN2), excluding several long-distance triplets with weak surface wave signal and low SNR. The results point generally to a significant fault damage zone at the southern part of JF array, between stations JFS3 and JF00, with Q_R values between 6 and 11. This is consistent with observations of fault zone trapped waves at these stations (Qiu *et al.* 2015). The northern two stations, JFN2 and JFN1, have higher Q_R values of ∼20 to 30. The results likely reflect attenuation in the top 30 m of the crust (again roughly estimated based on 1/3 of the

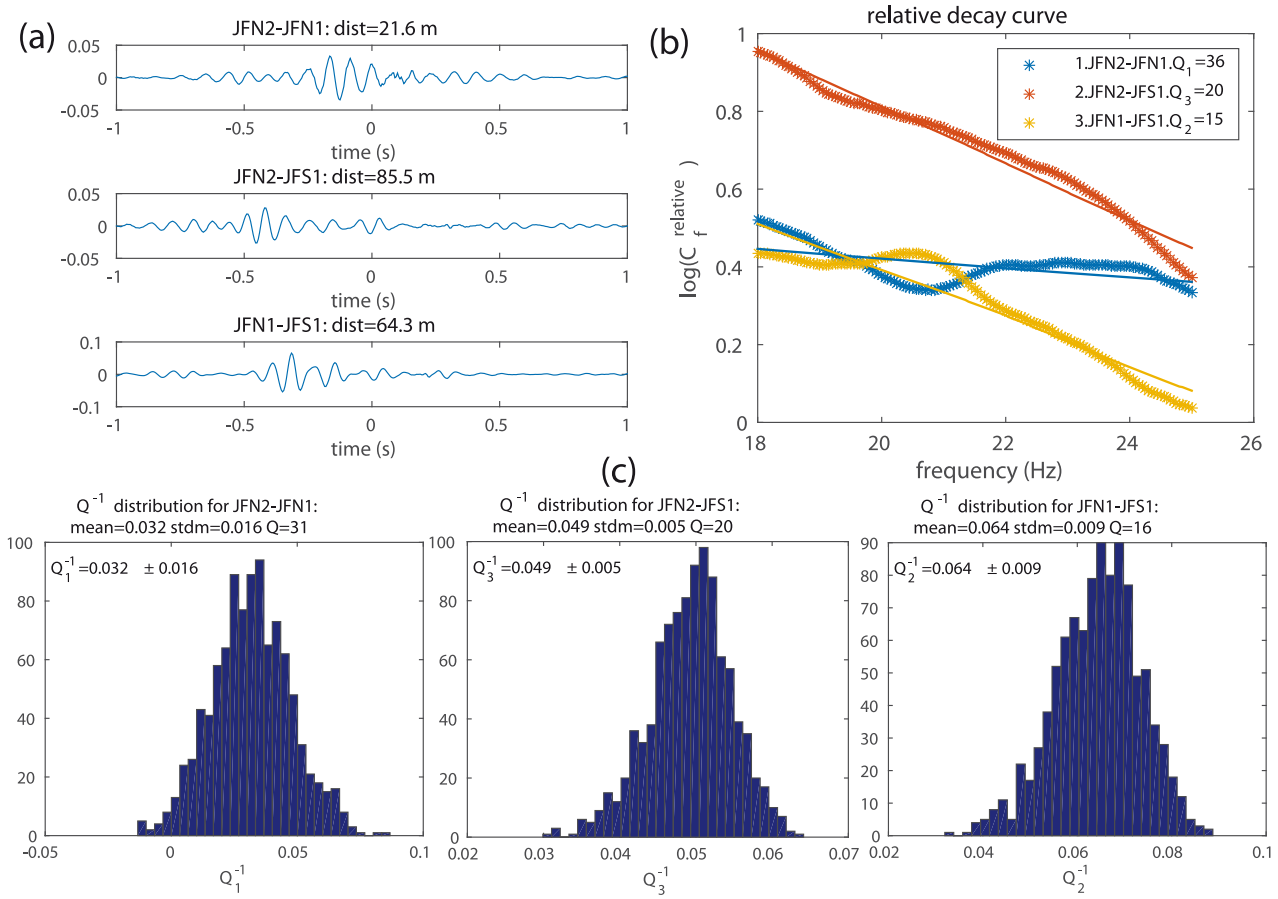

Figure 11. Cross-correlation functions, amplitude measurements and inverse Q distribution for JFN2-JFN1-JFS1. (a) Cross-correlations for JFN2-JFN1-JFS1. Interstation distances are indicated in titles. (b) Relative amplitude decay curve. Best-fitting curves are plotted as solid lines with the same colour as data. The frequency range is 18–25 Hz. (c) Distribution of inverse Q values for the 3 station pairs in JFN2-JFN1-JFS1 based on bootstrapping statistics ($1/Q_1 = 0.032 \pm 0.016$; $1/Q_3 = 0.049 \pm 0.003$; $1/Q_2 = 0.064 \pm 0.009$).

dominant used wavelength). The derived Q_R values are in the same range of Q_P and Q_S results obtained from earthquake data recorded in two shallow boreholes in the area (Aster & Shearer 1991). The results between stations JFS3 and JF00 are slightly lower than Q_S values obtained by waveform inversions of trapped waves at the JF and nearby site (Lewis *et al.* 2005; Qiu *et al.* 2015), probably because the trapped waves results reflect average values in the top ∼3.5 km of the crust.

A bootstrap technique enables us to quantify the variability of the inverted Q^{-1} values over different combinations of days. The ambient noise wavefield has seasonal variations (e.g. Stehly *et al.* 2006; Hillers & Ben-Zion 2011; Zhan *et al.* 2013). This produces variations in amplitude spectra of ambient noise cross-correlation over 2–3 months for the ocean microseism band (∼0.05–0.2 Hz). There can be additional short-term variations for the amplitude of high frequency noise cross-correlation (∼15–25 Hz) included in our study. Assuming that the attenuation/velocity structure do not vary significantly within the time range of our data, the inverted attenuation Q^{-1} values should be stable for different resampling sets of days. The bootstrap results for both the high frequency linear array and the low frequency regional triplet suggest that most of the inverted Q^{-1} values have relatively narrow confidence intervals.

The requirement of constant or similar site amplification factors in the frequency range used for inversion for the three stations limits the choice of triplets because the three stations should not be located in very different geological units (e.g. one in thick sedimentary basin and the others in hard rock or on a mountain). Otherwise the effect of site amplification may not be cancelled properly in eq. (2). The linear triplet geometry is a limitation on the number of available paths from which we can get attenuation (compared to all paths among randomly located 3 stations). Nevertheless, as shown in the paper with examples from regional and fault zone arrays, the method can be applied to many stations over wide range of scales. In particular, the method is suitable for regularly spaced arrays on local or regional (e.g. USArray) scales where many triplets can be formed to cover the region of interest.

The dense linear array requires high frequency noise that samples the upper tens of meters of crust. The advantage of high frequency noise is that it requires less number of days for the cross-correlation to converge. One disadvantage is that body wave phases can have comparable amplitudes to fundamental Rayleigh waves at larger distances due to attenuation of surface wave noise, which could potentially bias amplitude measurements. For example, a body P wave appears on some of the cross-correlations with high apparent velocities and can affect the phase and amplitude measurements of the surface wave. We derive both ZZ and RR cross-correlation components for the high frequency noise and then select the RR component for amplitude measurements to minimize the effect of body P wave phases.

The essential signal pre-processing steps should be improved in future. It is desirable to have a processing scheme that preserves most information in the noise cross-correlation. Pre-whitening is

not included in our analysis, since it modifies the amplitude decay curve (Weemstra *et al.* 2014). Instead, a time domain normalization is performed by dividing each trace segment of the ambient noise by its total power before cross-correlation. This strengthens the stationary noise assumption which could enhance the convergence of cross-correlation. Earthquakes and other unwanted signals (e.g. human activity) should be carefully removed (here we use amplitude clipping for small events and remove segments with larger earthquakes). The clipping method cannot completely remove small earthquakes that can pollute the noise data. Numerous tiny events with small SNR cannot be detected and may cause bias on the amplitude estimates. Removing many earthquake segments will reduce the length of available data and make the cross-correlations slower to converge. Different steps of pre-processing procedures should be experimented to determine improved processing flow in the future.

In the inversion step, the quality of results suffer from artefacts due to filtering and windowing in the process of isolating the fundamental mode surface wave packet in the causal or anticausal parts. The filter and windowing function should be optimized to minimize these artefacts. Generally, the goal is to select only the fundamental mode surface wave packet based on frequency and velocity constraints without introducing distortion of amplitude spectra due to the transition band of filter. It is challenging to select the desired signals from cross-correlations due to potential overlaps with other surface wave modes, body waves and other unwanted energy. Improvements in various signal processing steps will be attempted in a future work.

ACKNOWLEDGEMENTS

The paper benefited from discussions with Robert A. Scholtz and David Okaya and comments from two anonymous referees and editor Michael Ritzwoller. The study was supported by the National Science Foundation (grant EAR-0908903).

REFERENCES

Aki, K., 1957. Space and time spectra of stationary stochastic waves, with special reference to microtremors, *Bull. Earthq. Res. Inst.,* **35,** 415–457.

Aster, R.C. & Shearer, P.M., 1991. High-frequency borehole seismograms recorded in the San Jacinto Fault Zone, Southern California, Part 2. Attenuation and site effects, *Bull. seism. Soc. Am.,* **81,** 1081–1100.

Ben-Zion, Y. *et al.*, 2015. Basic data features and results from a spatially-dense seismic array on the San Jacinto fault zone, *Geophys. J. Int.,* **202,** 370–380.

Boschi, L., Weemstra, C., Verbeke, J., Ekström, G., Zunino, A. & Giardini, D., 2013. On measuring surface wave phase velocity from station–station cross-correlation of ambient signal, *Geophys. J. Int.,* **192**(1), 346–358.

Boué, P., Roux, P., Campillo, M. & Briand, X., 2014. Phase velocity tomography of surface waves using ambient noise cross correlation and array processing, *J. geophys. Res.: Solid Earth,* **119**(1), 519–529.

Campillo, M., 2006. Phase and correlation in random' seismic fields and the reconstruction of the green function, *Pure appl. Geophys.,* **163**(2–3), 475–502.

Campillo, M., Sato, H., Shapiro, N.M. & Van Der Hilst, R.D., 2011. New developments on imaging and monitoring with seismic noise, *Comp. Rend. Geosci.,* **343**(8–9), 487–495.

Dziewonski, A., Bloch, S. & Landisman, M., 1969. A technique for the analysis of transient seismic signals, *Bull. seism. Soc. Am.,* **59**(1), 427–444.

Galetti, E. & Curtis, A., 2012. Generalised receiver functions and seismic interferometry, *Tectonophysics,* **532–535,** 1–26.

Gouédard, P., Roux, P., Campillo, M. & Verdel, A., 2008. Convergence of the two-point correlation function toward the Green's function in the context of a seismic-prospecting data set, *Geophysics,* **73**(6), V47–V53.

Hauksson, E. & Shearer, P.M., 2006. Attenuation models (QP and QS) in three dimensions of the southern California crust: inferred fluid saturation at seismogenic depths, *J. geophys. Res.,* **111,** B05302, doi:10.1029/2005JB003947.

Herrmann, R.B., 1973. Some aspects of band-pass filtering of surface waves, *Bull. seism. Soc. Am.,* **63**(2), 663–671.

Hillers, G. & Ben-Zion, Y., 2011. Seasonal variations of observed noise amplitudes at 2–18 Hz in southern California, *Geophys. J. Int.,* **184,** 860–868.

Hillers, G., Ben-Zion, Y., Landès, M. & Campillo, M., 2013. Interaction of microseisms with crustal heterogeneity: a case study from the San Jacinto fault zone area, *Geochem. Geophys. Geosyst.,* **14**(7), 2182–2197.

Lewis, M.A., Peng, Z., Ben-Zion, Y. & Vernon, F.L., 2005. Shallow seismic trapping structure in the San Jacinto fault zone near Anza, California, *Geophys. J. Int.,* **162**(3), 867–881.

Lin, F.-C. & Ritzwoller, M.H., 2011. Helmholtz surface wave tomography for isotropic and azimuthally anisotropic structure, *Geophys. J. Int.,* **186**(3), 1104–1120.

Lin, F.-C., Moschetti, M.P. & Ritzwoller, M.H., 2008. Surface wave tomography of the western United States from ambient seismic noise: Rayleigh and Love wave phase velocity maps, *Geophys. J. Int.,* **173**(1), 281–298.

Lin, F.-C., Tsai, V.C. & Ritzwoller, M.H., 2012. The local amplification of surface waves: a new observable to constrain elastic velocities, density, and anelastic attenuation, *J. geophys. Res.,* **117**(B6), B06302, doi:10.1029/2012JB009208.

Liu, X. & Ben-Zion, Y., 2013. Theoretical and numerical results on effects of attenuation on correlation functions of ambient seismic noise, *Geophys. J. Int.,* **194**(3), 1966–1983.

Nolet, G., 1987. *Seismic Tomography: With Applications in Global Seismology and Exploration Geophysics,* Vol. 5, Springer Science & Business Media, pp. 275–276.

Pedersen, H.A., Mars, J. & Amblard, P.-O., 2003. Improving group velocity measurements by energy reassignment, *Geophysics,* **68,** 677–684.

Prieto, G.A., Lawrence, J.F. & Beroza, G.C., 2009. Anelastic Earth structure from the coherency of the ambient seismic field, *J. geophys. Res.,* **114**(B7), B07303, doi:10.1029/2008JB006067.

Qiu, H., Ben-Zion, Y., Ross, Z.E., Share, P.-E. & Vernon, F., 2015. Internal structure of the San Jacinto fault zone at Jackass Flat from earthquake data recorded by a dense linear array, in *Abstract of the Annual SSA Meeting*, April 2015, Pasadena, CA.

Roux, P., Kuperman, W.A. & Group, N. others, 2004. Extracting coherent wave fronts from acoustic ambient noise in the ocean, *J. acoust. Soc. Am.,* **116**(4), 1995–2003.

Shapiro, N.M. & Campillo, M., 2004. Emergence of broadband Rayleigh waves from correlations of the ambient seismic noise, *Geophys. Res. Lett.,* **31**(7), L07614, doi:10.1029/2004GL019491.

Shapiro, N.M., Campillo, M., Stehly, L. & Ritzwoller, M.H., 2005. High-resolution surface-wave tomography from ambient seismic noise, *Science,* **307**(5715), 1615–1618.

Snieder, R., 2004. Extracting the Green's function from the correlation of coda waves: a derivation based on stationary phase, *Phys. Rev. E,* **69**(4), doi:10.1103/PhysRevE.69.046610.

Stehly, L., Campillo, M. & Shapiro, N.M., 2006. A study of the seismic noise from its long-range correlation properties, *J. geophys. Res.,* **111**(B10), B10306, doi:10.1029/2005JB004237.

Tsai, V.C., 2011. Understanding the amplitudes of noise correlation measurements, *J. geophys. Res.,* **116**(B9), B09311, doi:10.1029/2011JB008483.

Weaver, R.L., 2011. On the amplitudes of correlations and the inference of attenuations, specific intensities and site factors from ambient noise, *Comp. Rend. Geosci.,* **343**(8–9), 615–622.

Weaver, R.L., 2013. On the retrieval of attenuation and site amplifications from ambient noise on linear arrays: further numerical simulations, *Geophys. J. Int.,* **193**(3), 1644–1657.

Weaver, R.L. & Lobkis, O.I., 2004. Diffuse fields in open systems and the emergence of the Green's function (L), *J. acoust. Soc. Am.,* **116,** 2731.

Weemstra, C., Westra, W., Snieder, R. & Boschi, L., 2014. On estimating attenuation from the amplitude of the spectrally whitened ambient seismic field, *Geophys. J. Int.,* **197**(3), 1770–1788.

Yao, H., van Der Hilst, R.D. & De Hoop, M.V., 2006. Surface-wave array tomography in SE Tibet from ambient seismic noise and two-station analysis—I. Phase velocity maps, *Geophys. J. Int.,* **166**(2), 732–744.

Zhan, Z., Tsai, V.C. & Clayton, R.W., 2013. Spurious velocity changes caused by temporal variations in ambient noise frequency content, *Geophys. J. Int.,* **194,** 1574–1581.

Zhan, Z., Tsai, V.C., Jackson, J.M. & Helmberger, D.V., 2014. Ambient noise correlation on the Amery Ice Shelf, East Antarctica, *Geophys. J. Int.,* **196,** 1796–1802.

Zigone, D., Ben-Zion, Y., Campillo, M. & Roux, P., 2015. Seismic Tomography of the Southern California plate boundary region from noise-based Rayleigh and Love Waves, *Pure appl. Geophys.,* **172,** 1007–1032.

APPENDIX: DERIVATION OF CROSS-SPECTRUM FOR ISOTROPIC NOISE SOURCES AND ASYMMETRIC ATTENUATION STRUCTURE

We assume the two stations are symmetric about the origin of a coordinate system, which is the centre of a ring containing the isotropic noise sources in the far field. The background attenuation quality factor values in the West (Q_{outW}) and East (Q_{outE}) half planes, are slightly different (Fig. 1a). Based on eq. (5) in Liu & Ben-Zion (2013), we have

$$\begin{aligned}\mathrm{E}\left\{\mathrm{C}_{u_1u_2}\left(-\frac{x}{2},\frac{x}{2};\omega\right)\right\} &= \int_{R_{\min}}^{R_{\max}} R\,dR \int_0^{2\pi} \frac{1}{\sqrt{\Delta_1(\theta)\Delta_2(\theta)}}\mathrm{B}(R,\theta;\omega) \\ &\times \exp\left[i\omega\left(\frac{\Delta_1(\theta)}{\tilde{c}^*(\omega)}+\frac{-\Delta_2(\theta)}{\tilde{c}(\omega)}\right)\right]\mathrm{d}\theta, \qquad \text{(A1)}\end{aligned}$$

where $\mathrm{E}\left\{\mathrm{C}_{u_1u_2}\left(-\frac{x}{2},\frac{x}{2};\omega\right)\right\}$ is the expected cross-spectrum function, $\mathrm{B}(R,\theta;\omega)$ is the far-field noise source spectral density at polar coordinate location (R,θ) with central frequency ω, and $\Delta_1(\theta)$ and $\Delta_2(\theta)$ are distances from source at angle θ to receivers 1 and 2, respectively. R is the distance between the far field noise source and the origin. The interstation distance is x. The inverse complex phase velocity is defined the in a similar way as in Liu & Ben-Zion (2013): $1/\tilde{c}(\omega) = (1-\mathrm{i}\,\mathrm{sgn}(\omega)/2Q(\omega))/c(\omega)$, where Q is the attenuation quality factor.We assign different attenuation Q values to different regions: Q_{in} for interstation region, Q_{outW} for background attenuation in the west half plane and Q_{outE} for background attenuation in the east half plane (see Fig. 1a). With stationary phase approximation (Fig. 1b), only the noise propagating within the end-fire lobes (Roux *et al.* 2004; Snieder 2004) contribute constructively to the cross-correlation of which the causal part decay is determined by Q_{in} and Q_{outW} and the anti-causal part decay is determined by Q_{in} and Q_{outE}. We also assume the Fresnel approximation that source–receiver distances are much greater than the interstation distance. As a result, we have $\Delta_1(\theta) \approx R + x\cos(\theta)/2$ and $\Delta_2(\theta) \approx R - x\cos(\theta)/2$, where R is the average distance from noise sources to origin. By evaluating the integrals in eq. (A1) for two half planes, we arrive at

$$\begin{aligned}\mathrm{E}\left\{\mathrm{C}_{u_1u_2}\left(-\frac{x}{2},\frac{x}{2};\omega\right)\right\} &= \pi\mathrm{B}(\omega)\exp\left[-\omega\left(\frac{R}{c(\omega)\,Q_{outW}}\right)\right] \\ &\times\left\{J_0\left(\frac{\omega x\varepsilon_W}{c(\omega)}\right)-\mathrm{i}\,H_0\left(\frac{\omega x\varepsilon_W}{c(\omega)}\right)\right\} \\ &+\pi\mathrm{B}(\omega)\exp\left[-\omega\left(\frac{R}{c(\omega)\,Q_{outE}}\right)\right] \\ &\times\left\{J_0\left(\frac{\omega x\varepsilon_E}{c(\omega)}\right)+\mathrm{i}H_0\left(\frac{\omega x\varepsilon_E}{c(\omega)}\right)\right\}, \qquad \text{(A2)}\end{aligned}$$

where $\varepsilon_W = 1-\mathrm{i}\frac{\mathrm{sgn}(\omega)}{2}\left(\frac{1}{Q_{\mathrm{in}}}-\frac{1}{Q_{outW}}\right)$ and $\varepsilon_E = 1+\mathrm{i}\frac{\mathrm{sgn}(\omega)}{2}\left(\frac{1}{Q_{\mathrm{in}}}-\frac{1}{Q_{outE}}\right)$ are complex coefficients containing the attenuation Q factors. J_0 represents zero.th order Bessel function of 1st kind and H_0 represents zero.th order Struve function of 1st kind. This equation, when narrow-band filtered, shows two wave packets propagating from west and east directions, respectively.

We simplify eq. (A2) assuming that the interstation distance is greater than the wavelength: $2\pi x \gg \lambda$. As a result, we have $|\omega x\varepsilon_E/c(\omega)| \geq |\omega x/c(\omega)| \gg 1$. The Bessel function terms can be simplified

$$\begin{aligned}J_0\left(\frac{\omega x\varepsilon_E}{c(\omega)}\right)+i\mathrm{H}_0\left(\frac{\omega x\varepsilon_E}{c(\omega)}\right) &\approx J_0\left(\frac{\omega x\varepsilon_E}{c(\omega)}\right)+iY_0\left(\frac{\omega x\varepsilon_E}{c(\omega)}\right) \\ &= H_0^{(1)}\left(\frac{\omega x\varepsilon_E}{c(\omega)}\right), \qquad \text{(A3)}\end{aligned}$$

where $H_0^{(1)}$ represents zero.th order Hankel function of the 1st kind and Y_0 represents zero.th order Bessel function of 2nd kind. The Hankel function can be further simplified (e.g. Mathematics Handbook; Wikipedia; Boschi *et al.* 2013)

$$\begin{aligned}H_0^{(1)}\left(\frac{\omega x\varepsilon_E}{c(\omega)}\right) &\approx \sqrt{\frac{i2c(\omega)}{\pi\omega x\varepsilon_E}}\exp\left[i\frac{\omega x\varepsilon_E}{c(\omega)}\right] \\ &= \sqrt{\frac{i2c(\omega)}{\pi\omega x\varepsilon_E}}\exp\left[-\omega\left(\frac{x\,\mathrm{Im}(\varepsilon_E)}{c(\omega)}\right)\right]\exp\left[i\frac{\omega x}{c(\omega)}\right], \qquad \text{(A4)}\end{aligned}$$

where the three factors on the right-hand side are amplitude correction factor, attenuation exponential decay factor and wave propagation factor, respectively. Similarly, the Bessel function term representing wave traveling from west can be simplified as

$$\begin{aligned}J_0\left(\frac{\omega x\varepsilon_W}{c(\omega)}\right)-i\mathrm{H}_0\left(\frac{\omega x\varepsilon_W}{c(\omega)}\right) &\approx \sqrt{\frac{-i2c(\omega)}{\pi\omega x\varepsilon_W}} \\ &\times\exp\left[-\omega\left(\frac{-x\,\mathrm{Im}(\varepsilon_W)}{c(\omega)}\right)\right]\exp\left[-i\frac{\omega x}{c(\omega)}\right]. \qquad \text{(A5)}\end{aligned}$$

Substituting eqs (A3)–(A5) back to eq. (A2), we have

$$\begin{aligned}\mathrm{E}\left\{\mathrm{C}_{u_1u_2}\left(-\frac{x}{2},\frac{x}{2};\omega\right)\right\} &= \pi\mathrm{B}(\omega)\sqrt{\frac{i2c(\omega)}{\pi\omega x\varepsilon_W}} \\ &\times\exp\left[-\omega\left(\frac{R-x/2}{c(\omega)\,Q_{outW}}+\frac{x}{2c(\omega)\,Q_{\mathrm{in}}}\right)\right]\exp\left[-i\frac{\omega x}{c(\omega)}\right] \\ &+\pi\mathrm{B}(\omega)\sqrt{\frac{-i2c(\omega)}{\pi\omega x\varepsilon_E}} \\ &\times\exp\left[-\omega\left(\frac{R-x/2}{c(\omega)\,Q_{outE}}+\frac{x}{2c(\omega)\,Q_{\mathrm{in}}}\right)\right]\exp\left[i\frac{\omega x}{c(\omega)}\right] \qquad \text{(A6)}\end{aligned}$$

We arrive at eq. (1) by multiplying site amplification factors β_1 β_2 on eq. (A6).